

High Performance Voltage Tailorable Room-temperature Ca-metal Batteries

Huawei Song

Sun Yat-sen University <https://orcid.org/0000-0001-9091-2297>

Jian Su

Sun Yat-sen University

Chengxin Wang ( wchengx@mail.sysu.edu.cn)

Sun Yat-sen University

Article

Keywords: calcium metal, tailorable window voltage, anion-cation, relay insertion/extraction, rechargeable battery

Posted Date: October 8th, 2020

DOI: <https://doi.org/10.21203/rs.3.rs-75382/v1>

License:  This work is licensed under a Creative Commons Attribution 4.0 International License.

[Read Full License](#)

Abstract

Calcium metal battery as one of the promising alternatives beyond Li-metal technology is challenged by the lack of suitable cathodes with considerable energy performance, and stable Ca anode of long-term stability and lower polarization potentials for Ca-plating/stripping. Here, by recycling cellulose waste paper of wide sources in our daily life, we develop feasible cathodes for Ca-metal batteries of good high-voltage and wide-window-voltage adaptability (0.005-4.9 V vs. Ca/Ca²⁺), except for considerable energy performance (~517.5 Wh kg⁻¹ at 0.1 A g⁻¹). Meanwhile, through tailorabile Ca-plating/stripping potentials ($\Delta V = \sim 0.65$ V) induced by electrolyte modification, proof-of-concept Ca-metal batteries not only delivered enhanced storage capability (101 mAh g⁻¹ vs. 51 mAh g⁻¹ at 0.1 A g⁻¹ in the window voltage of 2.0-4.7 V) and cycling stability (~77% capacity retention for 100 cycles), but also simultaneously held high output average working voltage of ~3.2V.

Main Text

The research of Ca-based rechargeable batteries has been highly attractive due to low redox potential (Ca ~ -2.87 V vs. standard hydrogen electrode, SHE), small ionic radius similar with that of sodium (Ca²⁺ ~1.00 Å vs. Na⁺~1.02 Å), and high natural abundance and good eco-friendliness of the Ca element.¹⁻² Actually, early work about the deposition of Ca at several organic electrolytes revealed a film-controlled process impossible for application in room temperature circumstances.³ Later on, the surface film was confirmed as electron insulating passivation layer functioning as the solid electrolyte interphases (SEIs) in lithium ion batteries (LIBs), but initial porous and accessible for anions leading to continuous corrosion (verified as anion oxidation forming CaF₂ or CaH₂) of freshly exposed calcium and finally densifying as passivation layer insulative for both electrons and ions.⁴⁻⁷ The anion oxidation phenomenon could be alleviated at relatively high temperature or by changing the electrolyte salts from Ca(PF₆)₂, Ca(BF₄)₂, and Ca(BH₄)₂ to corresponding fluorinated alkyl borates.^{4, 8-9} However, due to this issue arising from the character of calcium itself, it still needs long-term collaboration from both electrolyte chemistry and calcium-metal surface/interface engineering to fundamentally solve this bottleneck problem as that in lithium-metal technology.

Skipping calcium metal straight to its full batteries is currently a reasonable alternative strategy that are accelerating the pace of research on calcium-based battery technology. In this regard, the key is to screen suitable host materials for reversible Ca²⁺ insertion/extraction or adsorption/desorption reactions. For example, Prussian blue analogues, layered transition metal oxides and Van der Waals-bound layered transition metal sulfides featured with large tunnel structure or interlayer spacings have been reported as good cathodes, while tin, graphite carbon microbeads (MCMBs), and activated carbon cloth served as the anodes.¹⁰⁻¹⁶ For example, MnFe(CN)₆//calciated-Sn battery held a capacity of ~50 mAh g⁻¹ (based on the weight of the cathode) at 0-4 V after 30 cycles through a Ca²⁺/Na⁺ hybrid intercalation mechanism.¹⁰ A reversible capacity of ~ 75 mAh g⁻¹ due to Ca²⁺ insertion/extraction at 0.01-2V stably persisting for 100

cycles was reported for Na-doped ammonium vanadium oxide ($\text{NH}_4\text{V}_4\text{O}_{10}$) cathode and Ni-based framework anode system.¹² In particular, Mai's group presented a $\text{Mg}_{0.25}\text{V}_2\text{O}_5 \cdot \text{H}_2\text{O}$ /activated carbon cloth Ca-ion battery demonstrating high capacity retention ~87% for 500 cycles (~61 mAh g⁻¹) at 0.1 A g⁻¹ in the window voltage of -2.0-1.4 V.¹⁵ Despite important progresses, an obvious shortcoming is the low operation voltage, even below zero, due to inappropriate anodes and sluggish kinetics quite different from that of LIBs. Fortunately, through assembling dual-ion batteries, the low working voltage issue can be largely improved by utilizing the high voltage for anion insertion/extraction reaction.¹⁷ The representative work, which utilized the insertion of Ca^{2+} into the expanded graphite cathode and Sn-Ca alloying reaction in the anode, was carried in Tang and Chen's group.² The type Ca-ion batteries verified high window voltage of 3.0-5.0 V, impressive average working voltage above 4 V, and an initial capacity of 72 mAh g⁻¹ at 0.1 A g⁻¹, in spite of the apparently fluctuated cycling stability and coulombic efficiencies to be improved.² And hence, it is essential to search new cathodes to further improve the storage capability and cycling stability. In combination, it's still a long run to realize practical Ca-metal batteries in accompanying with severe challenges from fast degenerated plating/stripping and insertion/extraction chemistries and their sluggish kinetics and severe polarizations.^{7,18}

Here, we developed an inexpensive, freestanding membrane cathode of fast charge-kinetics by recycling cellulose waste paper. Except for high anodic stability up to 4.9 V, the cellulose waste paper derived graphitic carbon (CWPDG) cathodes also exhibited high storage capability up to 410 mAh g⁻¹ at 0.1 A g⁻¹, equivalent to a high energy capability of 517.5 Wh kg⁻¹. Through electrolyte optimization, the polarization potential for Ca-plating/stripping was reduced by ~0.65 V, meanwhile the CWPDG Ca-metal batteries with tailorble window voltages and stable cycling performance were also readily realized.

Results And Discussion

Recycling cellulose waste paper to graphitic carbon membrane

Before pyrolysis, a predegradation process was carried for the cellulose waste paper collected from the lab in order to get hydrocellulose with higher O content for Oxygen-doping. The purities mainly of Ca^{2+} , Mg^{2+} were eliminated by dilute hydrochloric aqueous solution (0.1 M HCl). As seen in **Figure S 1a**, uniform paper pulp would be achieved by redispersing the treated cellulose waste paper in deionized water, and CWPDG membranes were prepared by annealing the paper membranes gotten from vacuum filtration of the paper pulp (**Figure S 1b and 1c**). The powder X-ray diffraction (XRD) pattern of CWPDG (**Figure 1a**) exhibited two wide peaks at 22.2° and 43.6° (2q) ascribed to the diffraction of (002) and (101) planes for graphite-2H structure (PDF No. 41-1487). The marked shift of the peak for (002) planes diffraction to lower 2q indicates an enlarged lattice spacings (0.39 nm vs. 0.34 nm for standard graphite) which is attributed to deformed layers for sp_2 hybrid carbon due to O-doping common for various carbohydrates derived carbon nanostructures.¹⁹⁻²⁰ The scanning electron microscope (SEM) images (**Figure 1b and 1c**) showed CWPDG appeared as flexible fibre skeletons with the length of several hundred microns and width of a few microns coiled from waved nanosheets. The high angle annular dark

field scanning transmission electron microscope (HAADF-STEM) image (**Figure 1d**) verified the nanosheets full of nanopores. O-doping was also proved in the energy dispersive X-ray (EDX) spectrum (**Figure 1e**) with only C and O elements in the graphitic carbon. Clear diffraction rings in the select area electron diffraction (SAED) image (**Figure 1f**) attributed to the diffraction of (002), (101), and (110) planes substantiated its polycrystalline graphite-2H structure, which was also confirmed by the well-defined lattice fringes of ~2-5 layers in the high resolution transmission electron microscope (HRTEM) image (**Figure 1g**) characteristic of a layer spacing of ~0.39 nm analyzed by the fast fourier transform (FFT) and intensity profiles of the selected crystallized zones (**Figure 1h and 1i**) conforming to the XRD result.

Primary CWPDGC Ca-metal batteries and the electrochemical mechanism

To assemble primary Ca//CWPDGC batteries, tape casting electrodes of CWPDGC and the membranes were used as the cathodes, while commercial Ca was used as the anode. The electrolyte (denoted as Ca-soaked electrolyte) was made by forced ion exchange between fresh Ca and 1M LiPF₆ ethylene carbonate (EC)/diethyl carbonate (DEC) (v/v=1:1) electrolyte. The components of Ca-soaked electrolyte was roughly determined by the EDX spectrum of a drop electrolyte drying on a silicon wafer. As shown in **Figure S2**, Ca²⁺ amounts to ~7.8% (at.%) among all the cations of Li⁺ and Ca²⁺ according to the calculation based on the content of P. At first, the batteries were galvanostatically tested at a constant window voltage like LIBs. A high initial discharge capacity of 306.3 mAh g⁻¹ was obtained at 0.2 A g⁻¹ in a window voltage of 0.005-4.5 V, however, it quickly run out in less than 100 cycles (**Figure S3a**). Even if the current rate rised to 0.5 A g⁻¹, only 14% capacity was retained after 100 cycles (164 mAh g⁻¹ vs. 23 mAh g⁻¹). To address this issue, we also carried the test at constant charge durations. Specifically, at the current rates of 20 mA g⁻¹ and 200 mA g⁻¹, the current rates of 20 mA g⁻¹ and 200 mA g⁻¹, the primary Ca//CWPDGC batteries delivered high reversible capacities of 186 mAh g⁻¹ and 106 mAh g⁻¹ respectively when the upper voltage approached 4.9 V. The discharge profiles showed three different parts at around 4.73-1.80 V, 1.80-0.73 V, and 0.73-0.005 V which were consistent with the cathodic peaks ~ 3.88 and 3.08 V, 1.73 and 0.60 V, and 0.32 and 0.03 V correspondingly in the differential capacity curves (**Figure 2b**). Importantly, the impressive capacity lasted reversibly for 50 cycles at 20 mA g⁻¹ with the coulombic efficiencies roughly around 100% (**Figure 2c**). Moreover, the large storage capability was also held at various current rates. Specifically, high energy density of 517.5, 433.2, 251.4, and 86.7 Wh kg⁻¹ were achieved at the rates of 0.1, 0.2, 0.5 and 1.0 A g⁻¹ (**Figure 2d**). These corresponded to impressive specific capacities of 410.5, 250.3, 100.8, and 41.5 mAh g⁻¹ respectively (**Figure S 3b and 3c**). The superior storage capability and energy performance are comparable to some most advanced energy storage devices including Al-based batteries and Sn-graphite Ca-ion batteries.^{2, 21-23} Enhanced cycling performance was obtained by performing series of charge durations from 28 to 34 minutes at 0.2 A g⁻¹ (**Figure S 3d**). The best cycling performance (**Figure 2e**) consisted of initial reversible capacity of ~113 mAh g⁻¹ (at 2nd cycle), good capacity retention of 90.2% for 100 cycles, and high coulombic efficiencies above 90.9%. Although obvious potential shift was observed in the voltage-time (inset view of **Figure 2e**) and discharge profiles (**Figure 2f, Figure S 3e and 3f**), the good cycling performance at such wide

window voltage has never been seen for other cathodes. Besides, steady average working voltage around 2.0 V and energy density above 200 Wh kg⁻¹ were held for more than 100 cycles for both the tests at 0.1 and 0.2 A g⁻¹ (**Figure 2g**).

Ex situ characterization of CWPDGC at various stages of charge/discharge (SOCs) were performed to explore the quite different electrochemistry process. As seen in the XRD patterns (**Figure 3a-c**), diffraction peak of (002) plane shifted to lower 2q range at initial discharge stage to 0.005 V (denoted as D-1st-0.005) due to insertion reaction of cations, i.e., Li⁺ and Ca²⁺ like that of Li⁺ intercalation into graphite or other carbon nanostructures happening in LIBs, which recovered at the subsequent stage of charge process (~2.5 V, denoted as C-1st-2.5) because of the extraction reaction of the intercalated cations.^{20, 24-25} In the meantime, Ca stripping and Li/Ca plating proceeded at the anode. For further stages charge to 4.9 V (denoted as C-1st-4.9), the diffraction peak increasingly shifted to lower 2q range again resulted from anions insertion reaction similar with dual-ion batteries (DIBs), meanwhile cations continued to plate on the Ca anode.^{23, 26-27} In subsequent discharge process to 2.0 V (denoted as D-2nd-2), intercalated anions took out of the graphitic layers, leading to the recovery of the diffraction peak. To further discharge to 0.005V (denoted as D-2nd-0.005), cation intercalation occurred repeatedly as the initial discharge. The regular shift of diffraction peak during charge/discharge can be also clearly observed in the corresponding contour color map of the XRD profiles. The variation of the element content for F, P, and Ca in the EDX spectra provided us indirect clues of the change of various ions (**Figure 3d-f**). The lowering of peaks for F and P elements in the depth of discharge below 64.5% reflected the extraction of , and afterwards, Ca²⁺ insertion was indicated by increasing intensity for the peak of Ca element in fully discharge depth to 100%. Since the ionic radius of lithium (~0.76 Å) is smaller than that of calcium (~1.00 Å), it's reasonable to conclude that Ca insertion was accompanied by the insertion of Li, although we could't present the variation of Li element limited by the characterization technique.^{1, 7, 28}

Relating the cathodic peaks mentioned above with the analysis in XRD and EDX results, we can readily concluded that the cathodic peaks at 3.08 and 3.88 V was resulted from extraction reaction of adsorbed in surface or intercalated in graphitic layers, while the peaks at 1.73, 0.6, 0.32, and 0.03 V were attributed to adsorption or intercalation reaction from Li⁺ and Ca²⁺ respectively. Moreover, the relay insertion/extraction of cations and anions consisting of adsorption-desorption and intercalation/de-intercalation chemistry processes were also demonstrated in the ex situ HAADF-STEM, element mapping, and HRTEM images (**Figure 4**). At D-1st-0.005 stage (**Figure 4a-e**), obvious gathering of Ca element was observed in the mapping images, and the initial layer spacing of 0.39 nm for (002) planes was stretched to ~ 0.42 nm due to insertion of Ca²⁺ and Li⁺. In contrast, the color of Ca map changed lighter at C-1st-2.5 stage (**Figure 4f-j**), meanwhile the lattice spacing returned to ~0.39 nm after the extraction of Ca and Li. It's to note that the color of P and F maps didn't change obviously after insertion/extraction reaction of probably because of their poor discrimination and high content of F and P in the solid electrolyte interphases (SEIs), although the HRTEM images displayed severe change of lattice spacings from 0.39 nm to ~0.46 nm (**Figure 4k-t**). Comparing with the 1st discharge, larger lattice spacings were resulted (

~ 0.45 nm vs 0.42 nm) due to the ongoing activation by repeated insertion/extraction processes (**Figure 4u-y**).²⁹⁻³⁰ Overall, in the CWPDG Ca-metal batteries, both cations and anions are fully utilized through relay insertion/extraction mechanism quite different from that only cations in LIBs or anions in DIBs, which accounts for the higher storage capability.

Voltage tailorable CWPDG Ca-metal batteries

Except for the self-characters such as electropositivity, ionic radius, and charges etc., it's generally accepted that metal plating/stripping potentials are dependent on the solvation/desolvation properties, which are highly influenced by the ion concentration, type of solvents, substrates, and temperatures.^{7-8, 31-32} In the case of Ca-metal, the situations seem more complicated due to anion corrosion and large internal resistance resulted from the extremely insulative passivation layers.^{4-5, 7} Anyway, we found that the polarization potentials for Ca deposition/dissolution could be largely lowered through the increase of Ca^{2+} concentration by adding $\text{Ca}(\text{BF}_4)_2$. As shown in the potential-capacity profiles (**Figure 5a**), the potential for steady deposition of Ca happened at ~ -1.36 V (vs. Ca/Ca^{2+}) for Ca//Ca symmetrical cells with Ca-soaked electrolyte, which was increased by ~ 0.65 V when using Ca-soaked electrolyte with calcium tetrafluoroborate of 1% (weight ratio). According to the quantitative analysis based on the EDX spectrum (**Figure S4**), the content of Ca^{2+} roughly amounts to ~ 83.2 % (at.%) among all the cations in the modified electrolyte, which indicates an increase more than tenfold (vs. $\sim 7.8\%$). More importantly, they showed similar cycling stability up to nearly 400 hours with relatively smaller polarization potential shift (<300 mV) (**Figure 5b**).

Based on the change of Ca plating/stripping potentials being enabled by the electrolyte modification strategy, voltage tailorable CWPDG Ca-metal batteries with enhanced storage capability were readily realized. As shown by the typical voltage profiles (**Figure 5c**), the reversible capacities of 51 mAh g^{-1} at 2.0-4.7 V and 66 mAh g^{-1} at 1.15-4.60 V were raised to 101 mAh g^{-1} and 194 mAh g^{-1} respectively at 0.1 A g^{-1} after electrolyte modification. Moreover, the average working voltages have been also largely elevated up to ~ 3.2 V at the window voltage of 2.0-4.7 V (**Figure S5**).

Interestingly, the discharge profiles always displayed similar three characteristic features indicating the same cation-anion relay insertion/extraction mechanism no matter how the voltage has been tailored. The main disparity came from the boundary voltage dividing the cation insertion/extraction and anion insertion/extraction processes, which shifted to higher potentials as the lower cutoff voltage was elevated. The speculation was also revealed in the corresponding differential capacity curves (**Figure 5d**). Besides an elevation of the output energy (high voltage and superior storage capability), the cycling performance was also enhanced. After being tested at 100 mA g^{-1} for 100 cycles (**Figure 5e**), high capacities of $\sim 78 \text{ mAh g}^{-1}$ at 2.0-4.7 V and $\sim 123 \text{ mAh g}^{-1}$ at 1.15-4.60 V were maintained corresponding to retention of $\sim 77\%$ and $\sim 50\%$ respectively with enhanced coulombic efficiencies more than 93% after

the 20th cycle. Meanwhile, voltage tailorable CWPDG Ca-metal batteries also afforded to suffer successive fast-charge tests of 2 A g⁻¹, 1 A g⁻¹, 0.7 A g⁻¹, 0.5 A g⁻¹, and 0.2 A g⁻¹, more than 80-83% of the capacity could be output at 0.2 A g⁻¹ in the window voltage of 2.0-4.7 V (**Figure 5f**). Afterwards, the battery could stably run for more than 400 cycles at 0.2 A g⁻¹ and another 450 cycles at 0.1 A g⁻¹ with the capacity retention roughly above ~80% (~42 mAh g⁻¹). The impressive storage capability, energy performance, and excellent cycling stability should not only be attributed to the novel relay insertion/extraction for both cations and anions, but also be inseparable from the improved Ca plating/stripping processes and the more abundant free ions of Ca²⁺ which possess more favorable radius of polarization and molecular weight in comparison to .^{29-30, 33}

Methods

Materials. Cellulose waste paper collected from our lab was primarily degraded in deionized water under magneton stirring for one day. Pure paper pulp would be obtained by subsequently rinsing the degradation product with 0.1 M HCl aqueous solution for three times, and then deionized water and ethanol each time to eliminate the purities. Afterwards, the paper pulp was pumped into thin paper membranes by controlling its concentration and volume. After drying for 6h at 80°C, these paper membranes were pyrolyzed at 1000 °C under vacuum circumstance for 6 hours in a tube furnace with a heating ramp rate of 10 °C min⁻¹. CWPDG membranes would be achieved after natural cooling. Besides membranes themselves as electrodes, they were also pulverized in a degassed polyethylene (PE) bag for fabricating tape-casting electrodes used for electrochemical tests and mechanism characterization.

Ca-soaked electrolyte was made by repeatedly dipping fresh Ca plates in 1 M LiPF₆ EC/DEC (1:1, v/v) electrolyte for a week. 1% Ca(BF₄)₂ (w%) was added into Ca-soaked electrolyte to prepare the modified electrolyte (Ca-soaked electrolyte + 1% Ca(BF₄)₂).

Physicochemical characterizations. Microstructure, composition, and morphology of CWPDG and corresponding electrodes were characterized by thermal field emission SEM (Quanta 400F, 20 kV), field emission TEM (FEI Tecnai G2 F30, 300 kV), and EDX. Phase characterization was carried out on the powder X-ray diffractometer (XRD) (D/MAX 2200, Cu ka1, 5°/min). All the electrodes for characterization were washed with DEC to eliminate the residual electrolytes.

Electrochemical characterizations. For Ca//Ca symmetrical batteries, commercial Ca granules (99.9%, Sigma Aldrich) were pressed to plates (thickness, ~100-150 μm) which were directly used as both the working and counter electrodes. Ca-soaked electrolyte and its Ca(BF₄)₂ modified counterpart were used as the electrolytes, and glass microfiber filters (Whatman) were used as the separator. For Ca//CWPDG batteries, CWPDG membranes or CWPDG tape casting electrodes (with a weight ratio of CWPDG/PVDF=4/1) was tailored to an appropriate size and directly used as the cathodes, the weight was ~0.3-1 mg cm⁻². Standard cells (CR2032) with the above tailored electrodes, glass microfiber filter

separator, and 75 μL electrolyte were assembled in an Ar-filled universal glove box with the Oxygen and water vapor pressure less than 0.3 ppm.

The plating-stripping test of Ca//Ca symmetrical batteries were galvanostatically tested at 0.02 mA cm⁻² with the capacity of 0.06, 0.135 mAh cm⁻² respectively. The Ca// CWPDGC batteries were galvanostatically tested with various window voltage of 0.005-4.5 V, 0.005-4.9 V, 1.1-4 V, 1.15-4.6 V, and 2.0-4.7 V respectively. Cycling performance with different charge durations was also tested at a current density of 100 mA g⁻¹ and 200 mA g⁻¹ respectively. Fast-charge and long-term cycling performance test was also carried at varying rates from 2 A g⁻¹ to 0.1 A g⁻¹. All the tests were performed on a multichannel Neware battery testing system. Cells for mechanism analysis were galvanostatically discharged and/or charged to different cutoff voltages at 0.1 A g⁻¹.

References

1. Gummow, R. J.; Vamvounis, G.; Kannan, M. B.; He, Y., Calcium-Ion Batteries: Current State-of-the-Art and Future Perspectives. *Adv. Mater.* **2018**, *30*, 1801702.
2. Wang, M.; Jiang, C.; Zhang, S.; Song, X.; Tang, Y.; Cheng, H. M., Reversible calcium alloying enables a practical room-temperature rechargeable calcium-ion battery with a high discharge voltage. *Nat. Chem.* **2018**, *10*, 667-672.
3. Aurbach, D.; Skaletsky, R.; Gofer, Y., The Electrochemical Behavior of Calcium Electrodes in a Few Organic Electrolytes. *J. Electrochem. Soc.* **1991**, *138*, 3536-3545.
4. Ponrouch, A.; Frontera, C.; Barde, F.; Palacin, M. R., Towards a calcium-based rechargeable battery. *Nat. Mater.* **2016**, *15*, 169-72.
5. Lipson, A. L.; Proffit, D. L.; Pan, B.; Fister, T. T.; Liao, C.; Burrell, A. K.; Vaughey, J. T.; Ingram, B. J., Current Collector Corrosion in Ca-Ion Batteries. *J. Electrochem. Soc.* **2015**, *162*, A1574-A1578.
6. Song, H.; Su, J.; Wang, C., In Situ Subangstrom-Thick Organic Engineering Enables Mono-scale, Ultrasmall ZnO Nanocrystals for a High Initial Coulombic Efficiency, Fully Reversible Conversion, and Cycle-Stable Li-Ion Storage. *Adv. Energy Mater.* **2019**, *9*, 1900426.
7. Li, M.; Lu, J.; Ji, X.; Li, Y.; Shao, Y.; Chen, Z.; Zhong, C.; Amine, K., Design strategies for nonaqueous multivalent-ion and monovalent-ion battery anodes. *Nat. Rev. Mater.* **2020**, *5*, 276-294.
8. Wang, D.; Gao, X.; Chen, Y.; Jin, L.; Kuss, C.; Bruce, P. G., Plating and stripping calcium in an organic electrolyte. *Nat. Mater.* **2018**, *17*, 16-20.
9. Li, Z. Y.; Fuhr, O.; Fichtner, M.; Zhao-Karger, Z., Towards stable and efficient electrolytes for room-temperature rechargeable calcium batteries. *Energy Environ. Sci.* **2019**, *12*, 3496-3501.
10. Lipson, A. L.; Pan, B.; Lapidus, S. H.; Liao, C.; Vaughey, J. T.; Ingram, B. J., Rechargeable Ca-Ion Batteries: A New Energy Storage System. *Chem. Mater.* **2015**, *27*, 8442-8447.
11. Cabello, M.; Nacimiento, F.; González, J. R.; Ortiz, G.; Alcántara, R.; Lavela, P.; Pérez-Vicente, C.; Tirado, J. L., Advancing towards a veritable calcium-ion battery: CaCo₂O₄ positive electrode material.

Electrochim. Commun. **2016**, *67*, 59-64.

12. Vo, T. N.; Kim, H.; Hur, J.; Choi, W.; Kim, I. T., Surfactant-assisted ammonium vanadium oxide as a superior cathode for calcium-ion batteries. *J. Mater. Chem. A* **2018**, *6*, 22645-22654.
13. Wu, S.; Zhang, F.; Tang, Y., A Novel Calcium-Ion Battery Based on Dual-Carbon Configuration with High Working Voltage and Long Cycling Life. *Adv. Energy Mater.* **2018**, *5*, 1701082.
14. Lee, C.; Jeong, Y. T.; Nogales, P. M.; Song, H. Y.; Kim, Y.; Yin, R. Z.; Jeong, S. K., Electrochemical intercalation of Ca^{2+} ions into TiS_2 in organic electrolytes at room temperature. *Electrochim. Commun.* **2019**, *98*, 115-118.
15. Xu, X.; Duan, M.; Yue, Y.; Li, Q.; Zhang, X.; Wu, L.; Wu, P.; Song, B.; Mai, L., Bilayered $\text{Mg}_{0.25}\text{V}_2\text{O}_5 \cdot \text{H}_2\text{O}$ as a Stable Cathode for Rechargeable Ca-Ion Batteries. *ACS Energy Lett.* **2019**, *4*, 1328-1335.
16. Vo, T. N.; Hur, J.; Kim, I. T., Enabling High Performance Calcium-Ion Batteries from Prussian Blue and Metal–Organic Compound Materials. *ACS Sustainable Chem. Eng.* **2020**, *8*, 2596-2601.
17. Dahn, J. R.; Seel, J. A., Energy and Capacity Projections for Practical Dual-Graphite Cells. *J. Electrochim. Soc.* **2000**, *147*, 899-901.
18. Arroyo-de Dompablo, M. E.; Ponrouch, A.; Johansson, P.; Palacín, M. R., Achievements, Challenges, and Prospects of Calcium Batteries. *Chem. Rev.* **2020**, *120*, 6331-6357.
19. Song, H.; Yang, G.; Wang, C., General Scalable Strategy toward Heterogeneously Doped Hierarchical Porous Graphitic Carbon Bubbles for Lithium-Ion Battery Anodes. *ACS Appl. Mater. Interfaces* **2014**, *6*, 21661-21668.
20. Song, H.; Li, N.; Cui, H.; Wang, C., Enhanced storage capability and kinetic processes by pores- and hetero-atoms- riched carbon nanobubbles for lithium-ion and sodium-ion batteries anodes. *Nano Energy* **2014**, *4*, 81-87.
21. Lin, M. C.; Gong, M.; Lu, B.; Wu, Y.; Wang, D. Y.; Guan, M.; Angell, M.; Chen, C.; Yang, J.; Hwang, B. J.; Dai, H., An ultrafast rechargeable aluminium-ion battery. *Nature* **2015**, *520*, 324-328.
22. Kim, D. J.; Yoo, D. J.; Otley, M. T.; Prokofjevs, A.; Pezzato, C.; Owczarek, M.; Lee, S. J.; Choi, J. W.; Stoddart, J. F., Rechargeable aluminium organic batteries. *Nat. Energy* **2019**, *4* (1), 51-59.
23. Zhang, X.; Tang, Y.; Zhang, F.; Lee, C. S., A Novel Aluminum–Graphite Dual-Ion Battery. *Adv. Energy Mater.* **2016**, *6*, 1502588.
24. Buiel, E.; Dahn, J. R., Li-insertion in hard carbon anode materials for Li-ion batteries. *Electrochim. Acta* **1999**, *45*, 121-130.
25. Grout, H.; Kaplan, B.; Komaba, S.; Kumagai, N.; Gupta, V.; Nakajima, T.; Simon, B., Lithium Insertion into Carbonaceous Anode Materials Prepared by Electrolysis of Molten Li-K-Na Carbonates. **2003**, *150*, G67-G75.
26. Fan, L.; Liu, Q.; Chen, S.; Xu, Z.; Lu, B., Soft Carbon as Anode for High-Performance Sodium-Based Dual Ion Full Battery. *Adv. Energy Mater.* **2017**, *7*, 1602778.
27. Sheng, M.; Zhang, F.; Ji, B.; Tong, X.; Tang, Y., A Novel Tin-Graphite Dual-Ion Battery Based on Sodium-Ion Electrolyte with High Energy Density. *Adv. Energy Mater.* **2017**, *7*, 1601963.

28. Xiang, J. W.; Yang, L. Y.; Yuan, L. X.; Yuan, K.; Zhang, Y.; Huang, Y. Y.; Lin, J.; Pan, F.; Huang, Y. H., Alkali-Metal Anodes: From Lab to Market. *Joule* **2019**, *3*, 2334-2363.
29. Placke, T.; Heckmann, A.; Schmuck, R.; Meister, P.; Beltrop, K.; Winter, M., Perspective on Performance, Cost, and Technical Challenges for Practical Dual-Ion Batteries. *Joule* **2018**, *2*, 2528-2550.
30. Zhou, X.; Liu, Q.; Jiang, C.; Ji, B.; Ji, X.; Tang, Y.; Cheng, H. M., Strategies towards Low-Cost Dual-Ion Batteries with High Performance. *Angew. Chem., Int. Ed.* **2020**, *59*, 3802-3832.
31. Jie, Y.; Tan, Y.; Li, L.; Han, Y.; Xu, S.; Zhao, Z.; Cao, R.; Ren, X.; Huang, F.; Lei, Z.; Tao, G.; Zhang, G.; Jiao, S., Electrolyte Solvation Manipulation Enables Unprecedented Room-Temperature Calcium-Metal Batteries. *Angew. Chem., Int. Ed.* **2020**, *59*, 12689-12693.
32. Ta, K.; Zhang, R.; Shin, M.; Rooney, R. T.; Neumann, E. K.; Gewirth, A. A., Understanding Ca Electrodeposition and Speciation Processes in Nonaqueous Electrolytes for Next-Generation Ca-Ion Batteries. *ACS Appl. Mater. Interfaces* **2019**, *11*, 21536-21542.
33. Zhang, L.; Li, J.; Huang, Y.; Zhu, D.; Wang, H., Synergetic Effect of Ethyl Methyl Carbonate and Trimethyl Phosphate on BF_4^- Intercalation into a Graphite Electrode. *Langmuir* **2019**, *35*, 3972-3979.

Declarations

Acknowledgements

We acknowledge the support from the National Natural Science Foundation of China (nos. 51602355, 51872339, 91963210, and U1801255). H.W.S. also thanks the Basic Scientific Research Fund of Sun Yat-Sen University (no. 19lgpy02).

Author contributions

H.W.S. and C.X.W. designed and wrote the manuscript. H.W.S. and J.S. performed all the experiments of material synthesis, characterization, and cell performance tests. H.W.S. conducted the mechanism characterization, and all the authors discussed the results.

Correspondence and requests for materials should be addressed to C.X.W.

Competing financial interests

The authors declare no competing financial interest.

Figures

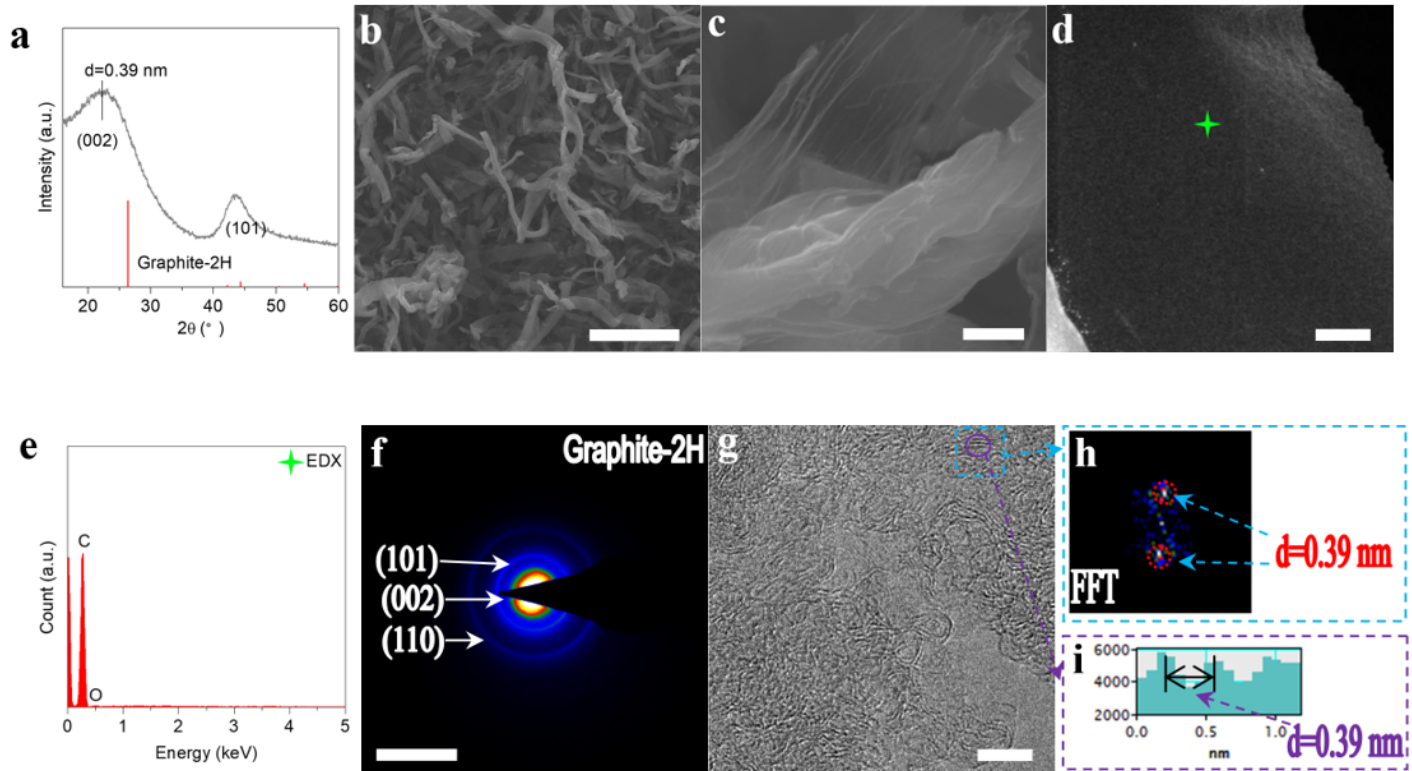


Figure 1

Microstructures of the CWPDGc. a) the XRD pattern in contrast to that of Graphite-2H, b, c) SEM images at different magnifications, d) HAADF-STEM image, e) EDX spectrum, f) SAED image, g) HRTEM image, and h) FFT and i) intensity profile of selected crystallized zone in g showing consistent lattice spacings of $\sim 0.39 \text{ nm}$. Scale bars, b) $50 \mu\text{m}$, c) $2 \mu\text{m}$, d) 100 nm , f) 10 nm , g) 5 nm .

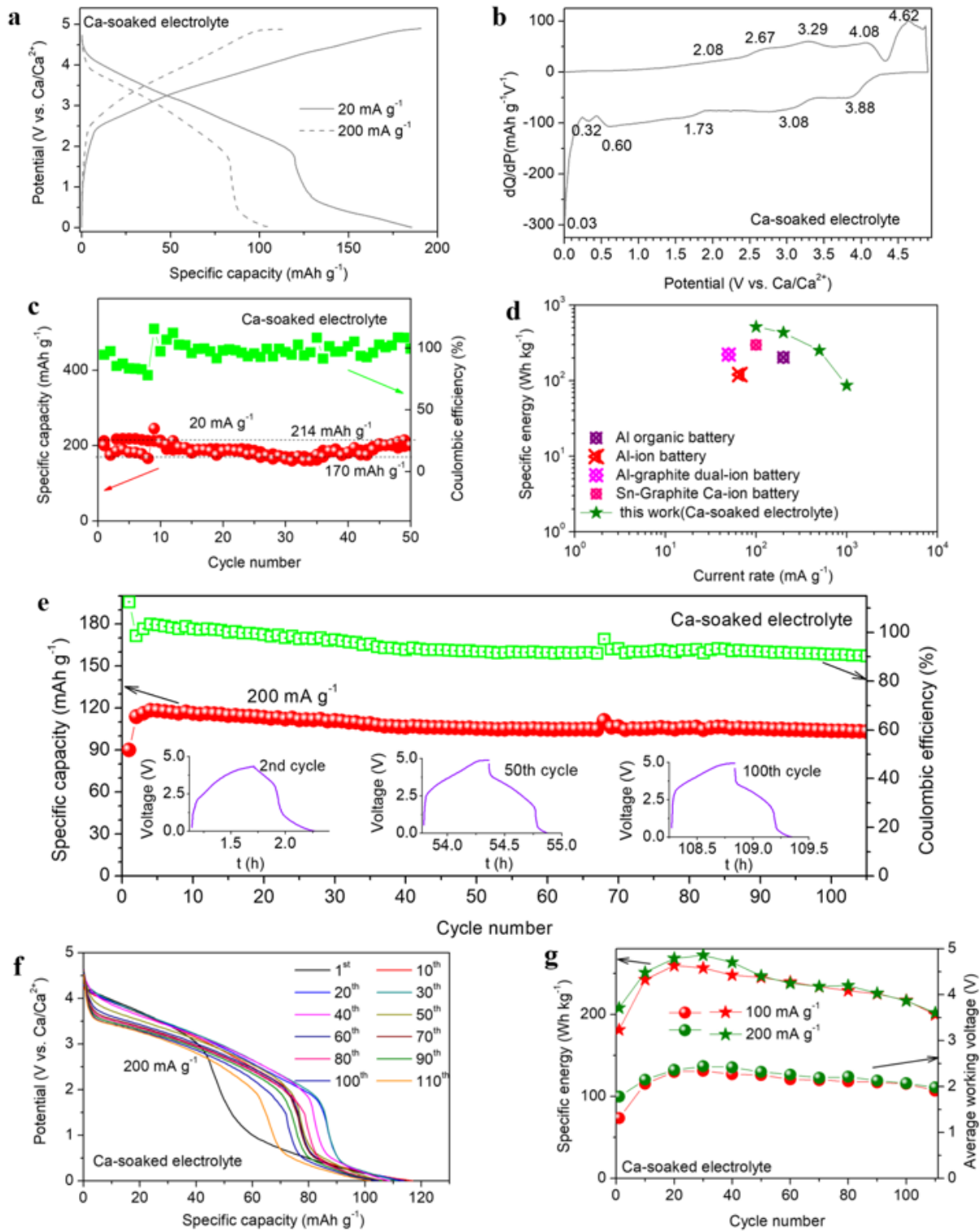


Figure 2

Ca//CWPDGC batteries at wide window voltages. a) typical voltage profiles at 20 and 200 mA g^{-1} , b) the corresponding differential capacity curve at 20 mA g^{-1} in the window voltage of 0.005-4.9 V, c) cycling performance at 20 mA g^{-1} , d) rate performance in contrast to other batteries, e) cycling performance and f) the corresponding discharge profiles, g) output energy performance and average working voltages at 0.1 and 0.2 A g^{-1} .

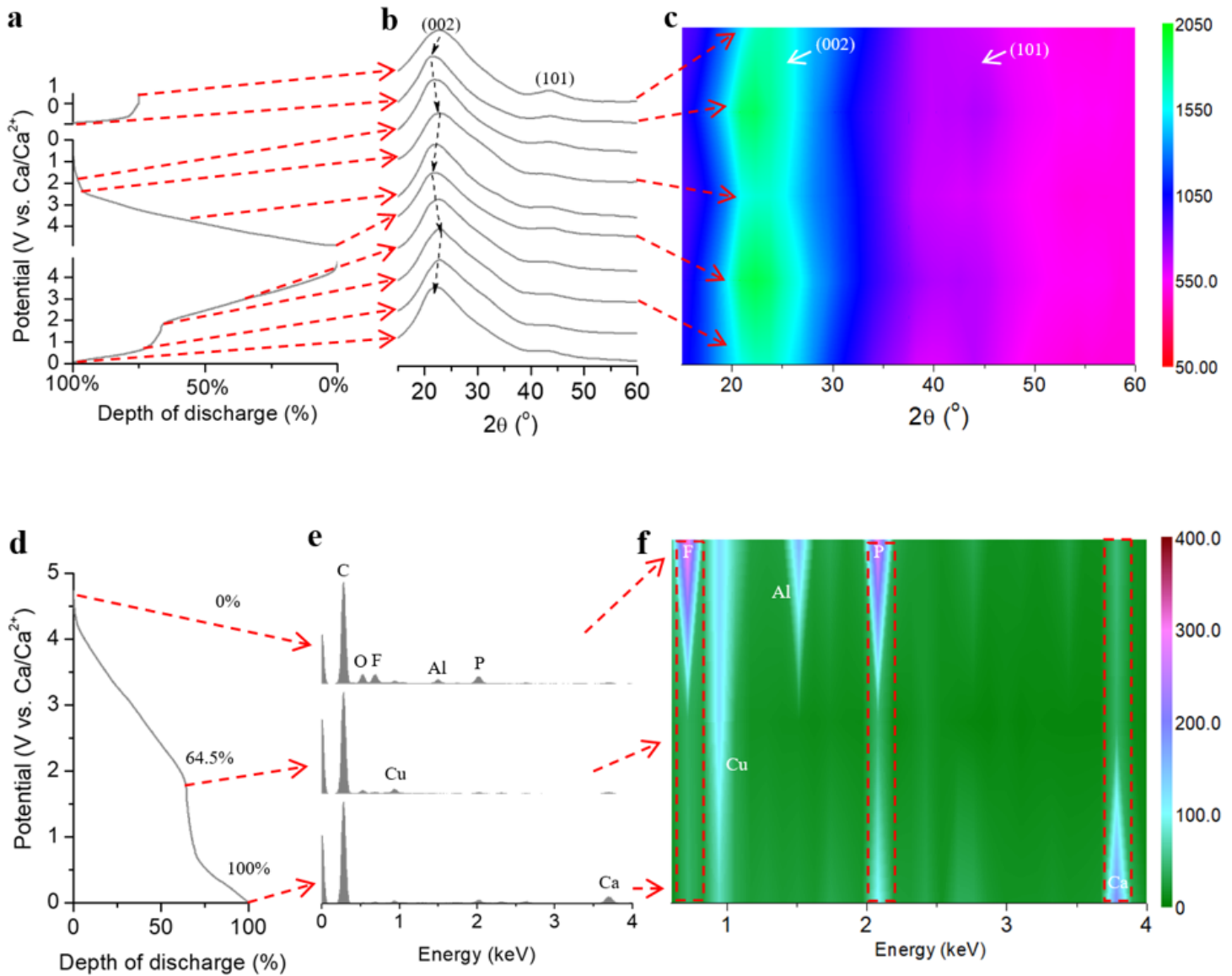


Figure 3

Ex situ structure characterizations of CWPDGC cathodes, a) voltage profiles with marked SOCs, b) the XRD profiles, and c) the corresponding contour color map of the XRD profiles, and ex situ element characterizations of WCPDGC cathodes, d) discharge profiles with marked SOCs, e) the EDX spectra, and f) the corresponding contour color map of the EDX spectra.

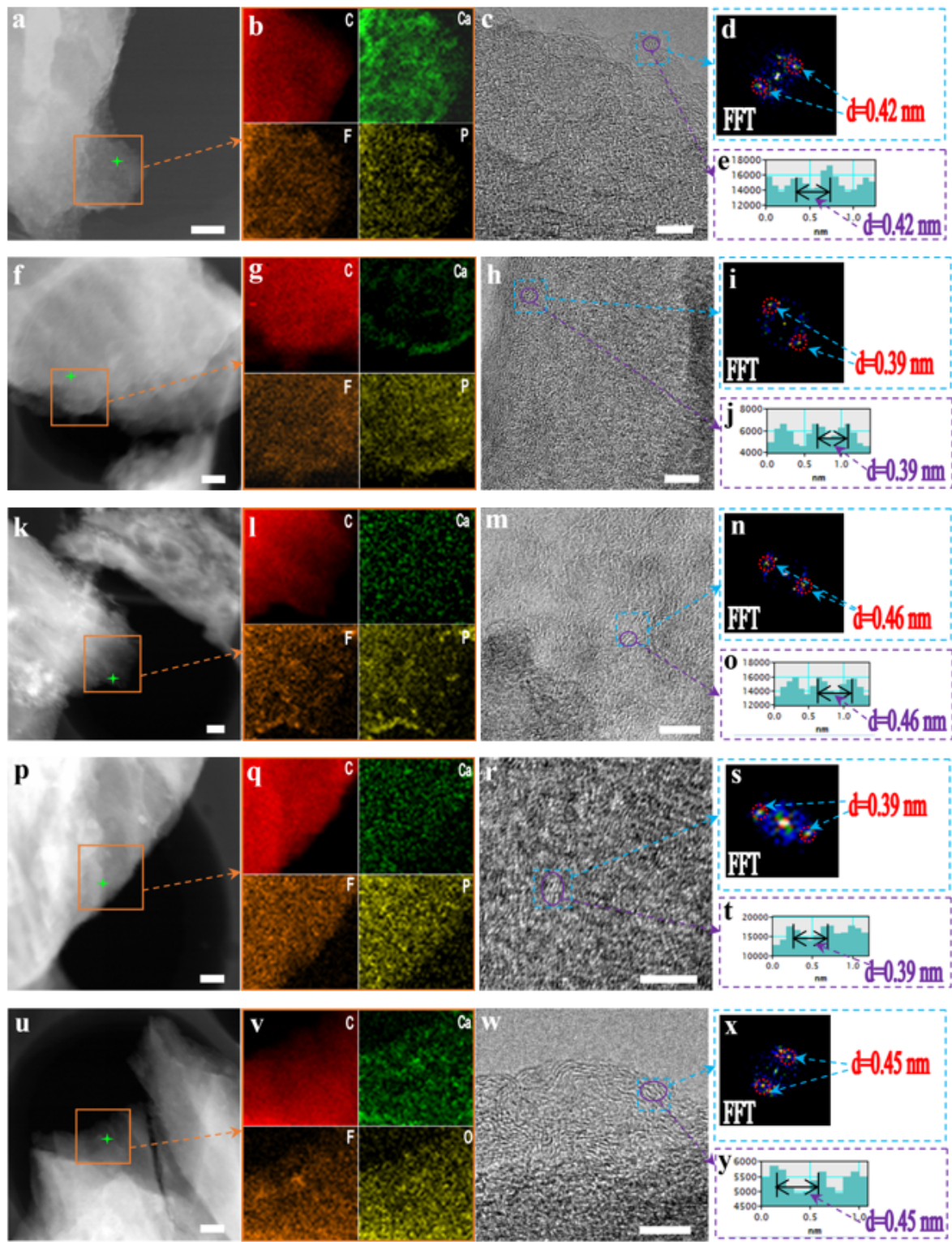


Figure 4

Ex situ microstructure characterizations of CWPDGC cathodes. HAADF-STEM image (scale bars: 200 nm), the element mapping images, the HRTEM images (scale bars: 5 nm) FFT and intensity profiles of selected crystallized zone in the HRTEM image, a-e) at the 1st discharge stage of 0.005 V (D-1st-0.005), f-j) at subsequent charge stage of 2.5 V (C-1st-2.5), k-o) at subsequent charge stage of 4.9 V (C-1st-4.9), p-

t) at subsequent discharge stage of 2.0 V (D-2nd-2.0), and u-y) at subsequent discharge stage of 0.005 V (D-2nd-0.005).

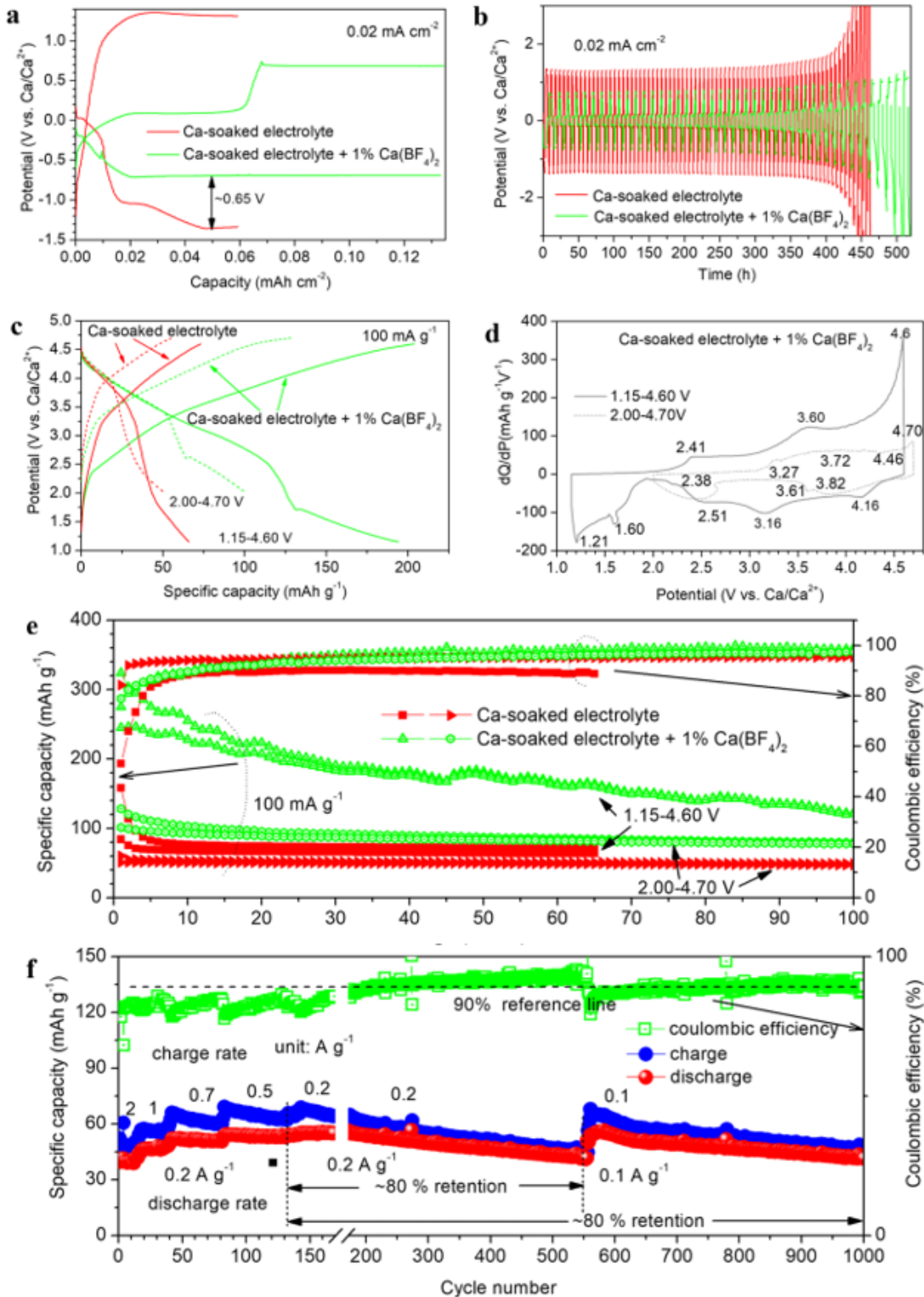


Figure 5

Ca//CWPDGC batteries at tailored window voltages. a) initial voltage-capacity profiles and b) voltage-time cycling for the plating-stripping processes of Ca-Ca symmetrical batteries, c) typical charge-

discharge profiles, d) differential capacity curves, e) cycling performance, f) fast-charge and long-term cycling performance.

Supplementary Files

This is a list of supplementary files associated with this preprint. Click to download.

- [SupportingInformation.docx](#)